Immediate and one-point roughness measurements using spectrally shaped light

XAVIER BUET*[1], MYRIAM ZERRAD[1], MICHEL LEQUIME[1], GABRIEL SORIANO[1], JEAN-JACQUES GODEME[2], JALAL FADILI[2] AND CLAUDE AMRA[1]

[1]*Aix-Marseille Univ, CNRS, Centrale Marseille, Institut Fresnel, Marseille, France*
[2]*Normandie Univ, ENSICAEN, CNRS, GREYC, France*
**xavier.buet@fresnel.fr*

Abstract: Capitalizing on a previous theoretical paper, we propose a novel approach different from the usual scattering measurements, one that is free of any mechanical movement or scanning. Scattering is measured along a single direction. Wide-band illumination with a properly chosen wavelength spectrum makes the signal proportional to the sample roughness, or to the higher-order roughness moments. Spectral shaping is carried out with gratings and a spatial light modulator. We validate the technique by crosschecking with a classical angle-resolved scattering set-up. Though the bandwidth is reduced, this white light technique may be of key interest for on-line measurements, large components that cannot be displaced, or other parts that do not allow mechanical movement around them.

© 2021 Optica Publishing Group under the terms of the Optica Publishing Group Open Access Publishing Agreement

1. Introduction

Light scattering from high quality optical coatings and substrates has been extensively studied for decades [1-6]. One of the first objectives was to reduce scattering in low-loss multi-dielectric mirrors involved in gyro-lasers systems. This has first led to huge improvements in polishing techniques which today allow to provide glass samples with roughness lower than a fraction of nanometer in the optical bandwidth [7-12]. The total integrated scattering from these super-polished substrates can be around a few ppm (1ppm = 10^{-6}) of the incident light. However, these surfaces are covered with multilayer thin films which may drastically increase the scattering. This increase originates from different processes which include the reproduction of substrate roughness layer after layer, the addition of residual roughness (including local defects) brought by the thin film materials during deposition, and the inhibited/enhanced interferences related to the multilayer design [6,13-17]. For that reason, a huge effort has been devoted to modern thin film deposition technologies (ion-assisted deposition, ion beam sputtering, magnetron sputtering, etc.) in order to produce thin films with high compactness that are insensitive to variations of the environment. With these technologies, the replication of substrate roughness within the multilayer has become the major component of light scattering, and hence creates a roughness and scattering threshold [16-17]. Note however that when the substrate roughness (and its replication) decreases, local defects distributed at low density on the sample surface may create another scattering threshold.

Within this context it can be agreed that all scattering improvements have relied on both a sophisticated metrology and a relevant theory. Integrated spheres [4,18] have been replaced by angle-resolved scatterometers [9,19-24] able to measure angular scattering at a single wavelength with 8-decades dynamics below a Lambertian scattering pattern. Despite these performances, these single wavelength scatterometers did not fit all requirements of optical coatings which are known to work in a wide wavelength range; indeed, one has to take into

account the spectral dispersion of roughness which is bandwidth dependent [6, 25-27]. For that reason, a few scatterometers were extended to multiple wavelengths [28-29] or to a wavelength continuum; the key difficulty of these optical systems was to hold an 8-decade dynamic over a wide spectral range [30-33] from the visible range to near-infrared.

Electromagnetic theories were developed in parallel to predict the angular and wavelength behavior of light scattering from optical coatings [6, 13-15, 34]. Bulk and surface theories were built and it was first shown that surface scattering is dominant for most materials and technologies [16-17]. Another outcome of these studies has highlighted the role of cross-correlation laws between interfaces, which drive the ability to produce interferences between waves scattered from different surfaces. This has led to the anti-scattering effect [35-36] now extended to loss minimization techniques in multilayer mirrors [37].

Today, this wealth of theoretical and experimental tools has eventually allowed scattering and roughness to be analyzed and characterized with high accuracy [38-39]. Analysis of uncoated opaque samples has become an easy task, which consists in extracting the roughness spectrum as the ratio of the measured data to a calculated scattering coefficient. Once the spectrum is determined, roughness is given by its integration in the bandwidth of the experiment. Results on uncoated substrates have been compared with other techniques such as atomic force microscopy, white light interferometry, scanning tunneling microscopy and photon scanning tunneling microscopy [25-26]. Such comparison has required to adjust the spatial frequency bandwidths of each system in order to take into account the roughness dispersion. Generally speaking, one can admit for optical applications that light scattering fits most characterization requirements, since the probe wavelength is the working wavelength.

Today, these techniques often meet new specifications. Indeed, all scatterometers involve a receiver, sample or beam motion to record the angular scattering pattern by reflection and transmission in the entire space. In some situations, these angular motions may present difficulties. This is the case when rapid measurements of roughness are required (on-line measurements), or when the sample cannot be displaced (e.g. large parts), or when only one scattering direction is allowed (e.g. where the sample cannot be separated from a system). For these reasons we recently proposed [40] an alternative which consists in using white light (i.e. light with a wide-band spectrum) so as to cancel any mechanical movement in a scattering system. The resulting system is a single-angle white-light scatterometer (WLS), which means that scattering is measured in a unique direction with a broadband illumination source. The bandwidth of spatial frequencies depends on the wavelength range of the illuminating beam, and is smaller than that of classical scatterometers. However, such systems still may be of great interest in the situations previously mentioned.

In this paper, and for obvious space limitation reasons, we restrict ourselves to a concise description of the theoretical basis that is sufficient to our purposes. The readers interested in a more comprehensive treatment or with a less strong background in scatter theory are invited to refer to [6]. The principle of this white light scatterometer (WLS technique), see [40], relies primarily on a wavelength/angle equivalence, where the two parameters (λ, θ) define the spatial frequency ($\nu \sim \sin(\theta)/\lambda$). However additional concepts must be introduced to make the white light scattering in one direction proportional to roughness, or to the higher-order roughness moments. Currently, we have to shape the illumination wavelength spectrum in a specific way given by the theory exposed in [40], and the scope of this paper is to present the experimental validation of this new technique.

Different techniques are available to shape the incident power spectrum. A first classical technique is based on interferential filters but suffers from drawbacks such as the absence of tunability or retroaction. A second technique [41] involves micro-mirror or LCD matrices coupled with gratings, offering three key advantages:

- The shaping can be adapted to an arbitrary source;
- Fast retroaction allows a shift in the source power spectrum to be taken into account;
- The tunability offers the opportunity to build quasi-arbitrary filters required for the higher-order roughness moments

Recall that the series of roughness moments δ_k (not only the roughness δ_0) may enable the autocorrelation function $\Gamma(\tau)$ of the surface topography to be retrieved, as in [27]:

$$\Gamma(\tau) = \sum_k (-1)^k \delta_{2k}^2 (\pi\tau)^{2k} \frac{1}{(k!)^2}. \quad (1)$$

For polished surfaces, a reasonable number of filters (less than 10) is sufficient for this function to be computed with high accuracy. We will discuss the advantages and limits of this WLS technique, schematically described in Fig. 1.

The paper is organized as follows. In section 2 we present generalized formulae which complement the approximate formulae given in the seminal paper [40]; this is a mandatory step for attaining greater accuracy in the roughness measurements. The experimental set-up is presented in section 3. We show in section 4 how the spectra are generated by spectral shaping [41]. In section 5 we present and discuss the results of the WLS experiment, and comparison with other techniques is given for validation. We conclude the paper in section 6.

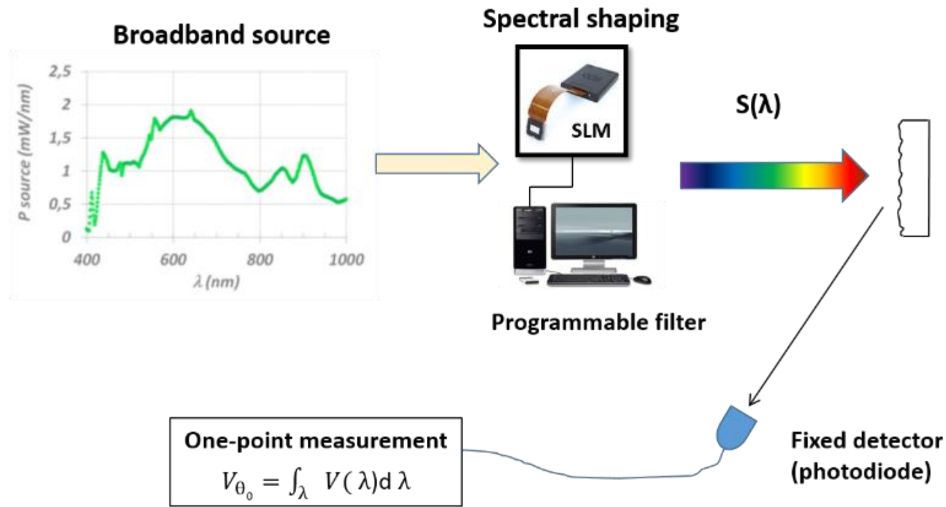

Fig. 1. Schematic description of the principle of the white light scattering experiment.

2. Principles underlying the WLS technique

For the sake of simplicity and to emphasize the WLS basic principles, approximate formulae were used in the seminal paper [40]. In the latter, it was assumed that the scattering coefficient $C(\theta, i, \lambda)$ had slight angular variations, allowing analytical formulae to be developed. Furthermore, the influence of incidence angle i was not addressed in detail. Preliminary experiments have shown that all these points must be corrected in order to achieve high precision in the roughness data. Hence we present below the generalized formulae that we propose in this work.

2.1 Scattering data at oblique illumination

Recall that the average sample normal is along a z-axis, so that the average roughness plane is (x,y). The scattered intensity I or angle-resolved scattering (ARS), is written as:

$$I(\theta_0, \lambda, i) = BRDF\cos(\theta) = C(\theta_0, \lambda, i)\gamma(\theta_0, \lambda, i), \tag{2}$$

with θ_0 the unique scattering direction, i the illumination incidence angle and $\gamma(\theta_0, \lambda, i)$ the sample roughness spectrum. $BRDF$ is known as the bidirectional reflection distribution function, analogous to a luminance. The scattering coefficient $C(\theta_0, \lambda, i)$ will not be developed since we use its exact form which is more complex, and can be found in [6, 34, 40]. This will change all formulae given in our paper [40]. Relation (2) yields, in terms of spatial frequencies $\vec{\nu}$:

$$I(\vec{\nu}, \vec{\nu}_0) = C(\vec{\nu}, \vec{\nu}_0)\gamma(\vec{\nu}, \vec{\nu}_0) = C(\vec{\nu}, \vec{\nu}_0)\gamma(\vec{\nu} - \vec{\nu}_0), \tag{3}$$

where $\vec{\nu}_0 = \left(\frac{n_0 \sin i}{\lambda}\right)\vec{x}$ is the incident spatial frequency. Hence in classical ARS scattering experiments the roughness spectrum is extracted as:

$$\gamma(\vec{\nu} - \vec{\nu}_0) = \frac{I(\vec{\nu}, \vec{\nu}_0)}{C(\vec{\nu}, \vec{\nu}_0)} = \gamma(\vec{\mu}), \tag{4}$$

so that the following frequencies $\vec{\mu}$ are explored:

$$\vec{\mu} = \vec{\nu} - \vec{\nu}_0 = (n_0/\lambda)\left|\begin{matrix}\sin(\theta)\cos(\varphi) - \sin(i) \\ \sin(\theta)\sin(\varphi)\end{matrix}\right. \tag{5}$$

with n_0 the refractive index of the measurement medium, and φ the polar or azimuthal scattering angle. Since we are working in the incidence plane, relation (5) becomes:

$$\vec{\mu} = (\nu - \nu_0)\vec{x}. \tag{6}$$

When the sample is rotated by an angle α around its normal [16,17], this rotating angle α must replace the polar angle φ in relation (5).

2.2 Spectral filter calculated with exact scattering coefficient

When illuminated with white light, the receiver at direction θ_0 delivers a voltage in the form:

$$V(\theta_0, i) = \Delta\Omega \int C(\theta_0, \lambda, i)\gamma(\theta_0, \lambda, i)F(\lambda)K(\lambda)d\lambda, \tag{7}$$

with $\Delta\Omega$ the solid angle, F(λ) the incident power spectrum of the source and K(λ) the spectral proportionality constant of the receiver. The roughness (or zero-order moment δ_0) is given by:

$$\delta_0^2(\theta_0, i) = \int \gamma(\vec{v})d\vec{v} = \int \gamma(v, \varphi)v dv d\varphi = 2\pi \int \bar{\gamma}(v)v dv, \quad (8)$$

where $\bar{\gamma}(v)$ is the average roughness spectrum over the polar scattering angle φ. This gives, in terms of wavelengths:

$$\delta_0^2(\theta_0, i) = 2\pi\, (n_0 sin\theta_0)^2 \int \bar{\gamma}(\theta_0, \lambda)d\lambda/\lambda^3. \quad (9)$$

According to (7) and (9), the voltage $V(\theta_0, i)$ will be proportional to the square of the roughness $\delta_0^2(\theta_0, i)$ provided we introduce a spectral filter T_η :

$$T_\eta(\theta_0, \lambda, i) = \frac{\eta(\theta_0,i)}{\lambda^3} \frac{1}{C(\theta_0,\lambda,i)F(\lambda)K(\lambda)}, \quad (10)$$

where the η constant is chosen to satisfy the condition $T_\eta \leq 1$. In practice, this parameter will be chosen to maximize the signal, which means that T_η will be unity at one wavelength.

The voltage then becomes proportional to the roughness, expressed in the form:

$$V_\eta(\theta_0, i) = \beta(\theta_0, i, \Delta\Omega)\, \delta_0^2(\theta_0, i), \quad (11)$$

with the constant: $$\beta(\theta_0, i, \Delta\Omega) = \eta(\theta_0, i)\Delta\Omega/[2\pi(n_0 \sin(\theta_0))^2]. \quad (12)$$

2.3 Roughness calibration

An etalon Lambertian sample is used for calibration in the presence of the filter T_η. For better accuracy, this etalon sample is illuminated at normal incidence for calibration. It delivers the voltage: $$V_L(\theta_0) = \Delta\Omega \int \rho(\lambda) \cos(\theta_0)\, F(\lambda)K(\lambda)T_\eta(\theta_0, \lambda, i)d\lambda, \quad (13)$$

where $\rho(\lambda) = \left(\frac{1}{\pi}\right)[1 - A(\lambda)]$ is the luminance of the etalon, whose absorption is usually negligible. Neglecting the absorption dispersion, and taking account of the transmission filter in (10), we obtain:

$$V_L(\theta_0) = \left(\frac{1}{2\pi}\right)\Delta\Omega[1 - A(\lambda)]\eta(\theta_0, i) \cos(\theta_0) \left[\frac{1}{b(\theta_0,i)}\right] \left[\lambda_{max}^2 - \lambda_{min}^2\right], \quad (14)$$

where $b(\theta_0, i)$ is related to the scattering coefficient as:

$$C(\theta_0, i) = b(\theta_0, i)/\lambda^4. \quad (15)$$

Note here that the substrate index dispersion was neglected, which makes the factor $b(\theta_0, i)$ non dispersive. Such an assumption is common but not necessary; where index dispersion needs to be considered, the integral (13) can be calculated numerically.

Forming the ratio of the voltages delivered by the sample under study $V_\eta(\theta_0, i)$ and those of the calibration sample $V_L(\theta_0)$, we get:

$$\delta_0^2(\theta_0, i) = \alpha(\theta_0, i) V_\eta(\theta_0, i)/V_L(\theta_0), \tag{16}$$

with the constant:

$$\alpha(\theta_0, i) = (n_0 \sin(\theta_0))^2 (1 - A) \ \cos(\theta_0) \ [1/b(\theta_0, i)][\lambda_{max}^2 - \lambda_{min}^2]. \tag{17}$$

This last constant is known at this stage, and allows the roughness from white scattering data in one direction to be extracted. Note that the numerical aperture of the optical fiber does not impact the procedure, since it is identical for sample and etalon measurements. Also, polarized scattering can be measured with the same procedure, provided that analyzers and polarizers are introduced in the optical system.

2.4 Procedures for higher-order roughness moments

Similar calculations and procedures must be developed for higher k-order roughness moments. These moments are defined as:

$$\delta_k^2(\theta_0, i) = 2\pi \int \nu^{k+1} \bar{\gamma}(\nu) d\nu, \tag{18}$$

so the filter that makes the scattering signal proportional to this moment is written as:

$$T_{\eta_k}(\theta_0, \lambda, i) = \frac{\eta_k(\theta_0, i)}{\lambda^{3+k}} \frac{1}{C(\theta_0, \lambda, i) F(\lambda) K(\lambda)}. \tag{19}$$

Filters of this kind (in the form of an inverse wavelength power) can be produced with the LCD matrix. The resulting voltage gives:

$$V_{\eta_k}(\theta_0, i) = \ \beta_k(\theta_0, i, \Delta\Omega) \delta_k^2(\theta_0, i), \tag{20}$$

With the constant : $\beta_k(\theta_0, i, \Delta\Omega) = \eta_k(\theta_0, i)\Delta\Omega/[2\pi(n_0 \sin(\theta_0))^{2+k}]$. (21)

The final step is to form the ratio of the voltages from the sample under study (V_{η_k}) to the etalon sample ($V_{L,k}$), that is:

$$\delta_k^2(\theta_0, i) = \alpha_k(\theta_0, i) V_{\eta_k}(\theta_0, i)/V_{L,k}(\theta_0). \tag{22}$$

Note again that both voltages are measured in the presence of the filter T_{η_k}. The constant is given by:

$$\alpha_k(\theta_0, i) = 2(n_0 \sin(\theta_0))^{2+k} (1 - A) cos\theta_0 \ [1/b(\theta_0, i)] \int d\lambda/\lambda^{k-1}. \tag{23}$$

The last integral is obtained immediately and depends on the k-order. At this stage it is worth stressing the fact that all quantities (roughness moments) depend on the frequency bandwidth related to the wavelength range (λ_{min}, λ_{max}) of the measurements.

3. Experimental set-up

Our experimental set-up is shown in Fig. 2. The white light source used in our experiment is a super-continuum laser (NKT EXB-6), and we select only the visible part of the spectrum using a splitter. This light is collimated with a broadband reflective collimator (ERC1), and then polarized (POL). Polarization is required here since our Spatial Light Modulator (SLM) comprises LCOS (Liquid Crystal on Silicon) cells that require the effects of polarization to adjust the level of the reflected light. A shutter (SH) is placed in the path of the beam and will be closed for recording the dark spectrum and dark current.

This collimated and polarized beam is then sent to a grating of 300 lines/mm to separate the wavelengths. An achromatic lens with a 7.5 cm focal length focuses the different spectral components onto the SLM and a lens and a grating symmetrically recombine all the wavelengths to generate the spectrally shaped beam. The gratings, lenses and SLM are placed in a 4f-setup. The SLM is an LCOS (Liquid Crystal on Silicon) matrix, reference LC-R 720, from HOLOEYE. It comprises 1280x768 pixels with a 20 µm pitch, giving an active area of 25.6x15.4 mm; addressing is 8 bit, corresponding to 256 grey levels. Another beam-splitter (BS) takes around 10% of this signal and sends it to the optical spectrum analyzer (OSA), which will contribute to the control of the emission spectrum. In between, the beam passes through optical density filters (ODs) to avoid saturation of the OSA. The OSA is a WASATCH PHOTONICS spectrometer based on a transmissive VPH grating with maximized efficiency.

Using a collimator (RRC1) and optical fiber (FOL2) with a core diameter of 200 µm, the beam is redirected to the scattering part of our experiment. It illuminates the sample, which scatters in all directions. We collect the scattered light with a reflective collimator (RRC2) placed at a fixed angle θ_0, and an optical fiber (FOL3, with a core diameter of 200 µm) connects it to our detector, a variable gain FEMTO-OE 200-SI photodiode, to obtain the voltage. The gain can be remotely varied between 10^3 and 10^{11}, and the output signal is digitized by a 16-bit NATIONAL INSTRUMENTS USB-6211 acquisition card.

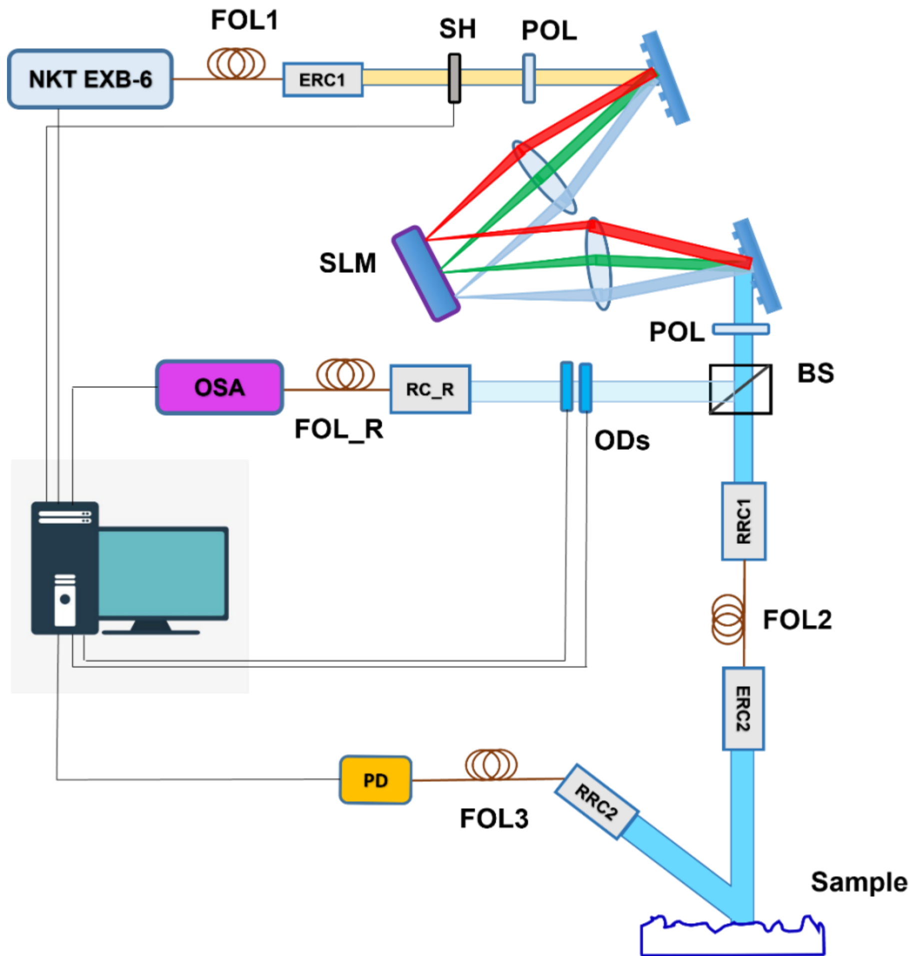

Fig. 2. Schematic representation of the white light scattering set-up (NKT EXB-6: super-continuum laser source; FOL1: fiber optic link 1; ERC1: emission reflective collimator 1; SH: shutter; POL: polarizer; SLM: spatial light modulator; BS: beamsplitter; ODs: optical density filters; RC_R: reference reflective collimator; FOL_R: reference fiber optic link; OSA: optical spectrum analyzer; RRC1: receiving reflective collimator 1; FOL2: fiber optic link 2; ERC2: emission reflective collimator 2; RRC2: receiving reflective collimator 2; PD: variable gain photodiode).

4. Generating the spectra

In this section we describe in detail how we generate the spectra required to recover the roughness moments. First of all, we present the SLM calibration, which needs to be carefully performed. We then describe the algorithm involving a feedback loop coded to obtain the target spectra.

4.1 SLM calibration

Our set-up requires two calibration steps: a calibration in wavelength, which associates a wavelength with each column, and a calibration in amplitude, allowing the quantity of light reflected by each column to be controlled.

Wavelength calibration is done by selecting a small number of columns and setting them to 1, all other columns being turned off. In our case, we consider 9 columns at each step, as this number gives a good compromise between the level of signal and the precision of the calibration. For each stack of 9 columns, we record the spectrum with the OSA, and a Gaussian fit gives the wavelength of the central pixel. The final result of this process is given in Fig. 3. We show that a 500 nm wavelength range between 520 nm and 1020 nm is spread over 600 columns, leading to a resolution of 0.8 nm/pix. In order to associate a wavelength with each column, we fit a 4th order polynomial to the measurement (blue curve). We observe that the wavelength distribution is almost linear, but a polynomial fit is nevertheless slightly more precise. In this figure we also represent (red curve with vertical scale on the right) the maximum intensity measured for each column. Using the 2 curves, we obtain a maximum power around 680 nm.

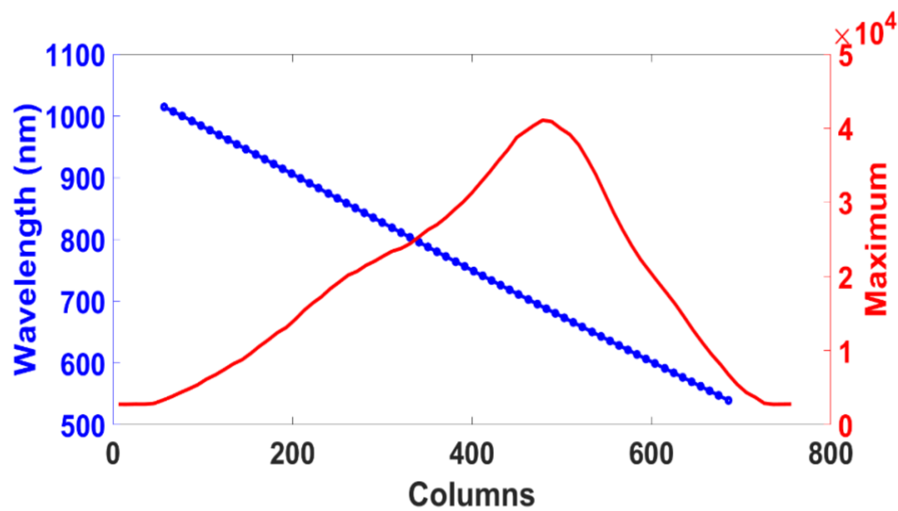

Fig. 3. Wavelength calibration of the LCOS matrix. Each wavelength is associated with one column (blue curve, left vertical scale). The spectral density of the incident power is plotted versus the columns (red curve, right vertical scale in arbitrary units).

The next step is the amplitude calibration. With our SLM, the level of each pixel is determined by entering in a matrix a value between 0 and 1. However, the measurement is not proportional to this value, so we need to establish the relationship between the entered value and the effect on the measurement. This can be done by setting the matrix to a constant value, and varying it between 0 and 1. Then for each spectral component, we extract the corresponding value from the measured spectrum, the final result being shown in Fig. 4. A 4th order polynomial fit gives very good agreement with our data. This relationship is wavelength dependent, and is thus established for each column.

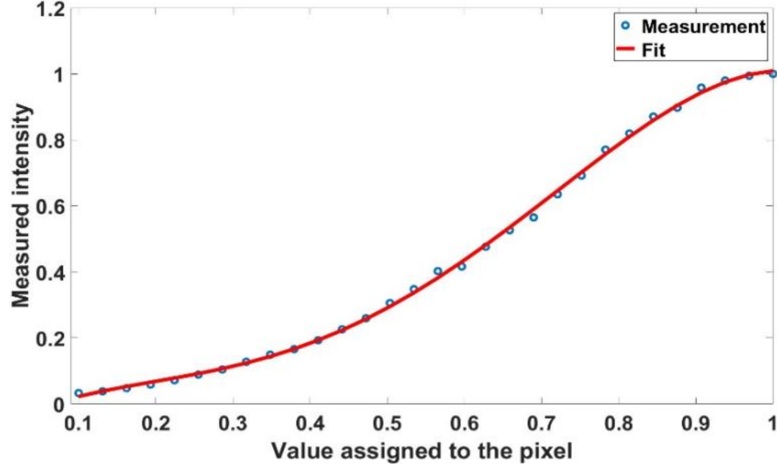

Fig. 4. Amplitude calibration of the LCOS matrix (see text)

4.2 Algorithm and results

Although the calibration is carried out with great precision, it always contains imperfections. This means that if we want to realize a defined shape of spectrum, it cannot be attained in just one step. We also want to take into account the temporal variations of the super-continuum laser. For these two reasons, the use of a feedback loop is necessary.

The algorithm draws considerably on [41], where it was used to flatten the spectrum of super-continua. No spectral shaping is applied to the initialization (all pixels set to 1). We record the first spectrum under these conditions, then allocate to each column a value for reaching the target spectrum in accordance with the amplitude calibration. A spectrum with these parameters is measured again, and from this new spectrum, we recalculate a spectrum without spectral shaping, i. e. we divide the measured spectrum by the coefficients given to the matrix during this iteration. Then we re-initiate the loop using this hypothetical spectrum as input. In practice, convergence occurs in approximately 15 iterations.

The spectrum displayed by the OSA already includes the emission spectrum of the source. Hence from (19) the target spectrum can be expressed as:

$$S_k(\lambda) = T_{\eta_k}(\theta_0, \lambda, i)F(\lambda) = \frac{\eta_k(\theta_0, i)}{\lambda^{k-1}} \frac{1}{b(\theta_0, i)K(\lambda)}, \quad (24)$$

where K is the spectral response of the receiver (we use a silicon photodiode). We also have to take into account the transmission coefficient of the optical densities and the reflectivity of the beam-splitter, since the part of the beam that illuminates the sample does not pass through these elements. In the text that follows, all spectra will be normalized to 1.

Fig. 5 shows the result of the algorithm and comparison with the target filter for the spectrum S_0 that will yield the roughness δ_0 of the sample. The agreement is very satisfactory in the range ($\lambda_{min} = 538\ nm; \lambda_{max} = 887\ nm$). We can still observe small oscillations on the spectrum due to instabilities in the super-continuum laser, but their intensity is too low to disturb the scattering measurements. Note that the spectral range of wavelengths ($\Delta\lambda = \lambda_{max} - \lambda_{min} = 349\ nm$) is limited mainly by the spectral response of the optical elements such as the

diffraction gratings or the LCOS matrix. Note also that the good agreement obtained in Fig.5 confirms that the optical fiber does not impact the shaping calibration procedure, due to its large core diameter (200 μm).

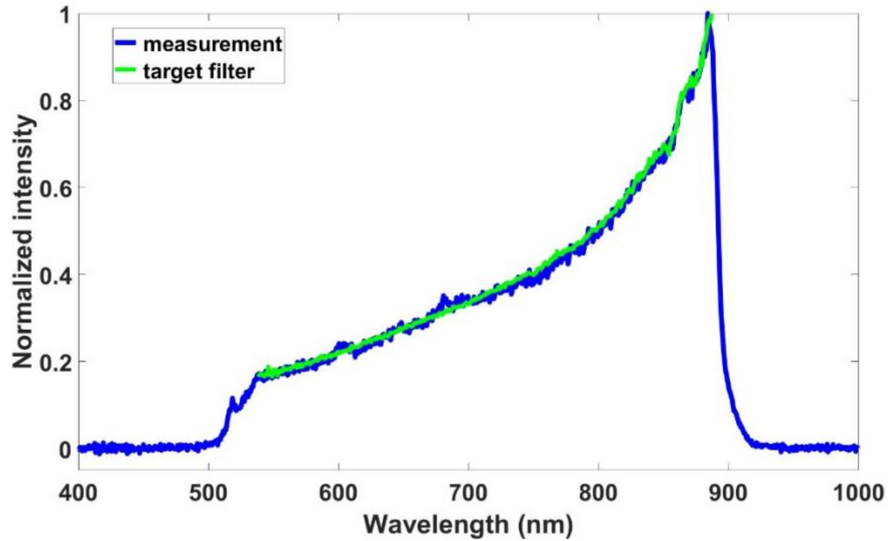

Fig. 5. Measured spectrum S_0 (blue) generated with the algorithm, compared with the target theoretical spectrum (green) - See text

Once this first spectrum is realized we increase the k-index of the spectra S_k and generate the next signals with the same procedure. Following relation (1), we are only interested in the even orders S_{2k}. As shown in Fig. 6, we obtain a very good agreement up to k=12. The targets plotted in Fig. 6 are S_2, S_4, S_6 and S_{14}. Above k=14, the noise floor of our experiment is reached, due to the specific dynamics in the spectral range. Hence under these experimental conditions, the number of accessible spectra is 6.

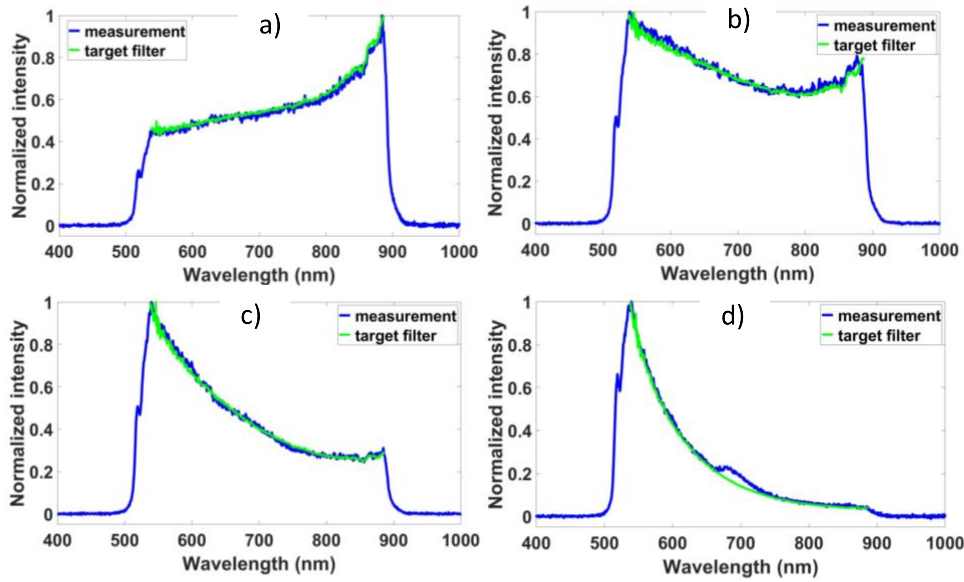

Fig. 6. Measured spectrum S_k generated with the algorithm (blue) and target theoretical spectrum (green) for different k values: a): k=2; b): k=4; c): k=6; d): k=14

5. Results and discussion

In this section we present the scattering measurements carried out with the spectrally shaped illuminating beams. The sample is a polished RG 1000 black glass sample with a real index in the visible range of around 1.55. This sample is opaque in the wavelength range [200 nm; 800 nm]; this opacity eliminates its back face in the scattering process, which provides easier investigation of the front face roughness for further comparison. Note that the imaginary index of the sample can be neglected in the scattering analysis, since the opacity is due to its great thickness (a few mm). This is valid because bulk scattering is known to be negligible in most optical substrates [34]. Following the previous sections, and taking into account the opacity range of the sample, we here use the WLS technique in the range [538 nm-800 nm] with normal and unpolarized illumination on the sample.

5.1 Results and comparison with zero-order roughness

We are first interested in the zero-order roughness moment δ_0 of the sample. Measurement is made using the WLS technique in direction $\theta_0 = 56°$, giving a roughness value of 4.8 nm for the polished sample. This measurement is immediate, as just one voltage is required to calculate the roughness. Note that since the incident beam is un-polarized, the scattering coefficient C of section 2 was taken as the half sum $(\frac{1}{2})(C_S + C_P)$ of the polarized coefficients.

It now remains to check this value with another scattering technique. To that end we crosschecked the WLS technique with a more classical multispectral Angle Resolved Scattering (ARS) measurement [25]. At this point it is necessary to stress the fact that roughness is bandwidth dependent [25-26]; theoretically a roughness moment is an integral over all spatial frequencies, but in practice it has limits determined by the experimental conditions. Hence the spatial frequency bandwidths of the WLS and the ARS techniques must be adjusted.

With classical ARS scatterometers (using angular scan at one wavelength λ, or at each consecutive wavelength), the bandwidth is:

$$BP_{ARS}(\lambda) = [\frac{\sin(\theta_{min})}{\lambda}, \frac{1}{\lambda}], \tag{25}$$

where θ_{min} is the minimum scattering angle close to specular reflection. In the case of the WLS technique at a fixed angle θ_0, this bandwidth is written as:

$$BP_{WLS}(\theta_0) = [\frac{\sin(\theta_0)}{\lambda_{max}}, \frac{\sin(\theta_0)}{\lambda_{min}}]. \tag{26}$$

We proceed as follows: with the SALSA set-up [32], ARS data are recorded at one visible wavelength λ. Though the set-up works in the range (400 nm-1.7 µm), the scattering data were recorded at λ=500 nm. The illumination incidence is i = 5°, with a minimum scattering angle of 5° from this reflected beam, that is, $\theta_{min} = 10°$. Such a minimum angle is enough for comparison with the WLS technique. Hence the angular range of ARS data is [10°; 90°]. Following relations (4-6) the roughness spectrum γ(ν) of the sample is extracted in the $BP_{ARS}(\lambda)$ bandwidth, as plotted in Fig. 7 (blue curve). Then using relations (8,18), we calculate the k-order roughness moments with these datas by integrating the function $\nu^{k+1}\gamma(\nu)$ in the WLS bandwidth $BP_{WLS}(\theta_0)$, so that the comparison becomes meaningful. This calculation is possible because the ARS range is greater than the WLS one, given the experimental conditions. The WLS technique is used at normal illumination. Note that since the incident beam of the SALSA set-up was un-polarized for this experiment, the scattering coefficients of section 2 were again taken as the half-sum $(\frac{1}{2})(C_S + C_P)$. Furthermore, these coefficients were calculated for the oblique incidence (5°) of the SALSA set-up.

Comparison in the same bandwidth between the two methods gives a SALSA roughness value of 4.3 nm, in acceptable agreement with the previous WLS roughness of 4.8 nm. The slight difference could be explained by the larger size of the WLS probe beam when the sample roughness is non-stationary. Anisotropy may also explain this difference, due to the fact that the angular position of the sample was not scanned.

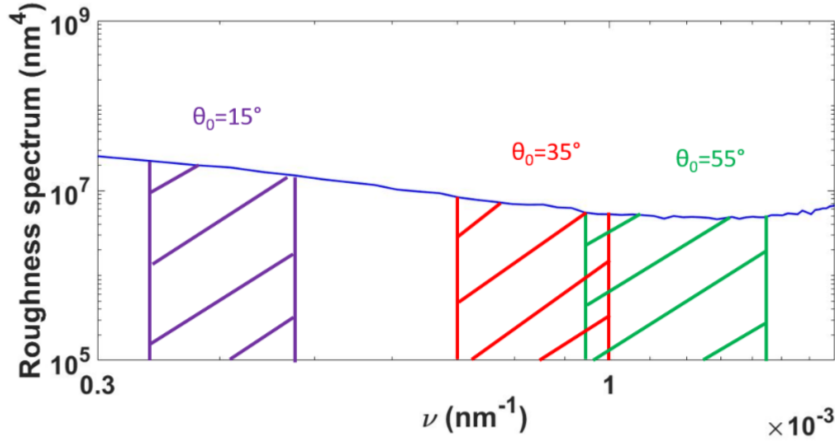

Fig. 7. Roughness spectrum of sample measured with the SALSA instrument (blue curve) at wavelength 500 nm. The WLS bandwidth is emphasized in color for different scattering directions. See text.

5.2 Further comparison at different angles of the WLS technique

We also performed this crosscheck for different angles θ_0 by manually moving the detector. Recall that the θ_0 angle alters the WLS bandwidth (see Fig. 7), which provides additional comparison with the ARS technique. Six θ_0 angles were considered in the range (15°; 70°) with an angular step of 10°. Each resulting WLS roughness $\delta_0(\theta_0)$ was then compared with the SALSA roughness by integrating $\nu\gamma(\nu)$ over the appropriate bandwidth $BP_{WLS}(\theta_0)$. Results are shown in Fig. 8. From the first angle to the last, the relative difference varies between 4% and 11%. The average value over the θ_0 angle is 4 nm with the WLS technique, and 3.8 nm with the ARS technique. These results confirm the good correspondence.

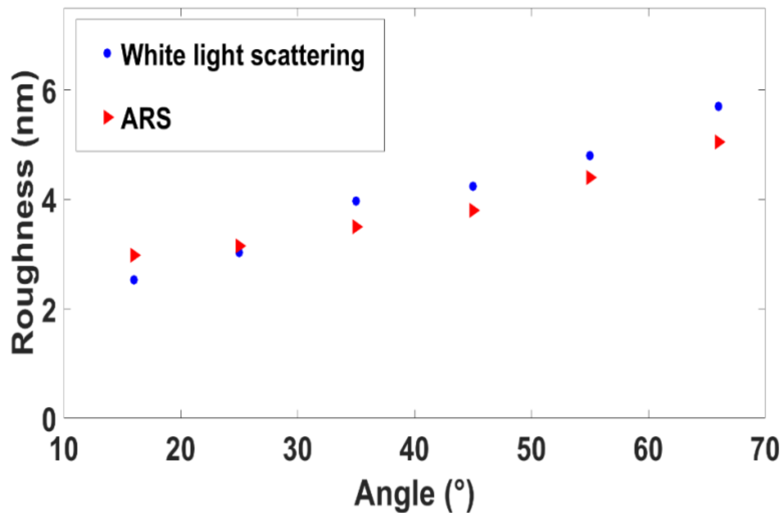

Fig. 8. Comparison of the roughness of the RG 1000 glass sample measured with the white light scattering technique at different θ_0 angles, and with the multispectral ARS SALSA instrument. All bandwidths were adjusted for the comparison (see text).

5.3 Results on the higher-order roughness moments

The last cross-checking between the two methods was carried out on the higher order roughness moments (Fig. 9-10). With the white light configuration, the kth order roughness moment is determined from the voltage ratio (see eq. 22-23) when the illuminating beam is shaped to get the spectrum S_k. A unique angle is here considered (see Fig.7). We chose $\theta_0 = 35°$ since it corresponds to a medium bandwidth, as shown in Fig.7. For the SALSA instrument, the moments were calculated by integrating $\nu^{k+1}\gamma(\nu)$ over the appropriate pass-band. Fig. 9-10 shows good agreement for the 6 other moments that were obtainable with the WLS technique. The difference between the two methods is less than 10%. To provide an accurate comparison, in Fig. 9 we plotted the ratio of the roughness moments obtained by the two techniques. In Fig.10 the two roughness moments are plotted to emphasize their absolute values. Note that δ_2 gives the root mean square of the sample slope.

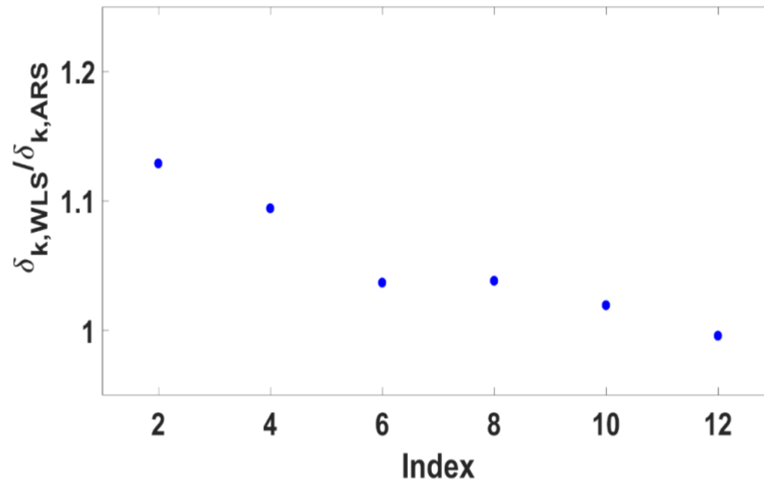

Fig. 9. Value of the ratio between the roughness moments measured with the white light scattering set-up at an angle of 35°, and the roughness moments obtained with the multispectral ARS SALSA instrument.

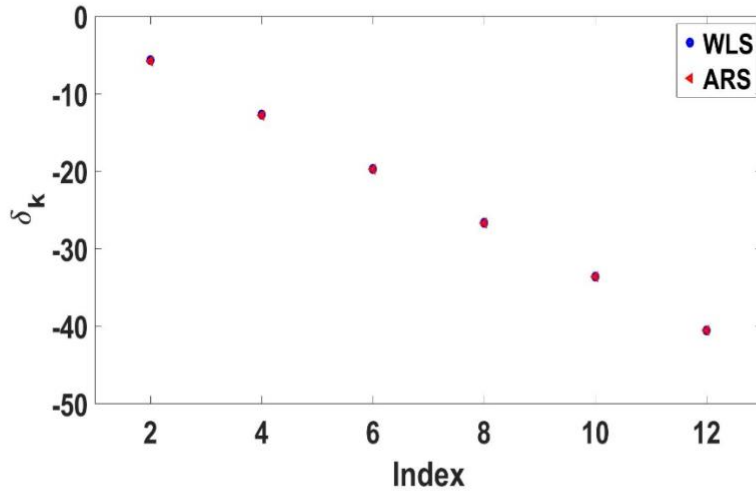

Fig. 10. Absolute values of the roughness moments measured by the ARS technique (red data) and the WLS techniques (blue data)

Before conclusion, it is interesting to stress the fact that, though the general discussion in this section has emphasized a successful comparison between the WLS and the SALSA techniques, some discrepancies (less than 10%) remain on the roughness moments. These differences are not attributed to bar errors since the relative and absolute accuracy of the scattering techniques lie around 1% in the spectral range. Hence it is more probable that they must be attributed to roughness anisotropy, due to the fact that all measurements were performed in the incidence plane, while the angular position of the sample was not checked from one technique (WLS) to another (SALSA). Also, the spot size is different in the two experiments, while the density of local defects is not uniform on the sample. We hope to improve the comparison in a future work thanks to the mounting of the sample on rotation and translation plates.

6. Conclusion

We have presented a new method for scattering measurements that requires no mechanical motion or wavelength scan. This is made possible by the use of white light (i.e. light with a wide-band spectrum) with defined spectra to illuminate the sample. These spectra were generated by spectral shaping, allowing us to create programmable filters that use retroaction and that take into account the temporal shift of the super-continuum laser. We have shown that, using these spectra, we could obtain immediate and reliable roughness measurements, validated by another ARS technique. The WLS technique also enables higher-order roughness moments of the sample to be obtained by shaping specific spectra. All results are quasi-instantaneous. The trade-off to the gain in speed and flexibility is a reduced range of spatial frequencies. This method should prove useful in industry for testing large or immovable samples, or for on-line measurements, or where angular motion around the sample is not possible. It may find applications in space, microelectronics, biology or security.

Note that the WLS pass-band could be broadened with a wider spectral range; for instance, 3 frequency decades would be provided between 400 nm and 1200 nm, but this would require optical elements with broader spectral responses. Note also that there is no ideal pass-band to characterize the roughness (the wider the better), unless the application (optical, mechanical, chemical, etc.) is specified and its pass-band of interest can be identified. The WLS technique

provides roughness moments δ_k at different k-orders, providing an alternative to the roughness spectrum data $\gamma(\nu_q)$.

It should also be noted that this WLS technique is for now limited to uncoated substrates. Addressing the case of multilayers would require to replace the scattering coefficients by a sum of numerous scattering coefficients weighted by different roughness spectra and cross-correlation laws between roughnesses [6].

7. Funding, acknowledgments, and disclosures

The authors thank the French National Research Agency (ANR) for funding the project FIRST (ANR-19-CE42-0009). They also thank Marin Fouchier for the scattering data measured with the SALSA scatterometer.

The authors declare no conflicts of interest.

The datasets presented in this paper are available from the corresponding author upon reasonable request.

References:

1. S. O. Rice, ''Reflection of electromagnetic waves from slightly rough surfaces'', Commun. Pure Appl. Math. 4(2-3), 351–378 (1951).
2. J. M. Eastman, "Surface scattering in optical interference coatings," J. Opt. Soc. Am. 66, 164–164 (1976).
3. J.W. Goodman, "Laser Speckle and Related Phenomena" (Springer-Verlag, 1984).
4. Jean M. Bennett and Lars Mattsson, "Introduction to Surface Roughness and Scattering", (Optical Society of America, 1989)
5. John C. Stover, Optical Scattering: Measurement and Analysis, Third Edition, (SPIE Press, 2012).
6. C. Amra, M. Lequime and M. Zerrad, "Electromagnetic Optics of Thin-Film Coatings" (Cambridge University Press, 2021).
7. P. Roche and E. Pelletier, "Characterization of optical surfaces by measurement of scattering distribution", Appl. Opt. 23(20), 3561–3566 (1984).
8. J. M. Elson, J. M. Bennett, and J. C. Stover, "Wavelength and angular dependence of light scattering from beryllium: comparison of theory and experiment," Appl. Opt. 32(19), 3362-3376 (1993).
9. P. Kadkhoda, A. Miller, D. Ristau, A. Duparré, S. Gliech, H. Lauth, U. Schuhmann, N. Reng, M. Tilsch, R. Schuhmann, C. Amra, C. Deumie, C. Jolie, H. Kessler, T. Lindstr?m, C.-G. Ribbing, and J. M. Bennett, "International round-robin experiment to test the International Organization for Standardization total-scattering draft standard," Appl. Opt. 39(19), 3321-3332 (2000).
10. T. A. Germer, C. Wolters, and D. Brayton, "Calibration of wafer surface inspection systems using spherical silica nanoparticles," Opt. Express 16(7), 4698-4705 (2008).
11. A. Duparré, J. Ferre-Borrull, S. Gliech, G. Notni, J. Steinert, and J. M. Bennett, "Surface characterization techniques for determining the root-mean-square roughness and power spectral densities of optical components," Appl. Opt. 41, 154-171 (2002).
12. J. E. Harvey, S. Schroder, N. Choi, and A. Duparre, "Total integrated scatter from surfaces with arbitrary roughness, correlation widths, and incident angles," Opt. Eng. 51(1), 013402 (2012).
13. J. M. Elson, J. P. Rahn, and J. M. Bennett, "Relationship of the total integrated scattering from multilayer-coated optics to angle of incidence, polarization, correlation length, and roughness cross-correlation properties," Appl. Opt. 22(20), 3207–3219 (1983).
14. J. M. Bennett, H. H. Hurt, J. P. Rahn, J. M. Elson, K. H. Guenther, M. Rasigni, and F. Varnier, "Relation between optical-scattering, microstructure and topography of thin silver films .1. Optical-scattering and topography," Appl. Opt. 24(16), 2701–2711 (1985).
15. A. Duparre and S. Kassam, "Relation between light-scattering and the microstructure of optical thin-films," Appl. Opt. 32(28), 5475–5480 (1993).
16. C. Amra, "From light scattering to the microstructure of thin-film multilayers," Appl. Opt. 32(28), 5481–5491 (1993).

17. C. Amra, "Light scattering from multilayer optics. II. Application to experiment," J. Opt. Soc. Am. A 11(1), 211–226 (1994).
18. S. A. Mann, B. Sciacca, Y. Zhang, J. Wang, E. Kontoleta, H. Liu, and E. C. Garnett," Integrating Sphere Microscopy for Direct Absorption Measurements of Single Nanostructures", ACS Nano 2017, 11(2), 1412–1418, (2017).
19. M. Lequime, M. Zerrad, C. Deumie, and C. Amra, "A goniometric light scattering instrument with high-resolution imaging," Opt. Commun. 282(7), 1265–1273 (2009).
20. S. Schroder, D. Unglaub, M. Trost, X. B. Cheng, J. L. Zhang, and A. Duparre, "Spectral angle resolved scattering of thin film coatings," Appl. Opt. 53(4), A35–A41 (2014).
21. M. Zerrad, M. Lequime, and C. Amra, "Far-field spatially angle-resolved scattering measurements: practical way to recover surface topography," Opt. Eng. 53(9), 092012 (2014).
22. A. von Finck, M. Trost, S. Schroder, and A. Duparre, "Parallelized multichannel BSDF measurements," Opt. Express 23, 33493–33505 (2015).
23. D. Kim, K. Y. Jeong, J.Kim, H. S. Ee, J. H. Kang, H..G. Park, and M. K. Seo, "Quantitative and Isolated Measurement of Far-Field Light Scattering by a Single Nanostructure, Phys. Rev. Applied 8, 054024 (2017).
24. M. Husnik, S. Linden, R. Diehl, J. Niegemann, K. Busch, and M. Wegener, "Quantitative Experimental Determination of Scattering and Absorption Cross-Section Spectra of Individual Optical Metallic Nanoantennas", Phys. Rev. Lett. 109, 233902 (2012).
25. P. Dumas, B. Bouffakhreddine, C. Amra, O. Vatel, E. Andre, R. Galindo, and F. Salvan, "Quantitative Microroughness Analysis down to the Nanometer Scale," Europhys. Lett. EPL 22, 717–722 (1993).
26. C. Deumie, R. Richier, P. Dumas, and C. Amra, "Multiscale roughness in optical multilayers: atomic force microscopy and light scattering," Appl. Opt. 35, 5583–5594 (1996).
27. BG. Hoover and PA. Reyes, "Extended-range AFM imaging for applications to reflectance modeling," Proc. SPIE 9961, 99610R (2016)
28. C. Amra, D. Torricini, and P. Roche, "Multiwavelength (0.4mm-10.6 mm) angle-resolved scatterometer or how to extend the optical window," Appl. Opt. 32(28), 5462–5474 (1993).
29. S. Schroder, M. Trost, T. Herffurth, A. von Finck, and A. Duparre, "Sophisticated light scattering techniques from the VUV to the IR regions," in Reflection, Scattering, and Diffraction from Surfaces Iii, L. M. Hanssen, ed. (2012), Vol. 8495.
30. M. Lequime, S. Liukaityte, M. Zerrad, and C. Amra, "Ultra-wide-range measurements of thin-film filter optical density over the visible and near-infrared spectrum," Opt. Express 23(20), 26863-26878 (2015).
31. Michel Lequime, Myriam Zerrad, and Claude Amra, "Breakthrough spectrophotometric instrument for the ultra-fine characterization of the spectral transmittance of thin-film optical filters," Opt. Express 26(26), 34236-34249 (2018)
32. Marin Fouchier, Myriam Zerrad, Michel Lequime, and Claude Amra, "Wide-range wavelength and angle resolved light scattering measurement setup," Opt. Lett. 45(9), 2506-2509 (2020)
33. S. Liukaityte, M. Lequime, M. Zerrad, T. Begou, and C. Amra, "Broadband spectral transmittance measurements of complex thin-film filters with optical densities of up to 12," Opt. Lett. 40(14), 3225 (2015).
34. C. Amra, C. Grezes-Besset, and L. Bruel, "Comparison of surface and bulk scattering in optical multilayers," Appl. Opt. 32(28), 5492–5503 (1993).
35. C. Amra, G. Albrand, And P. Roche, "Theory and Application of Antiscattering Single Layers - Antiscattering Antireflection Coatings," Applied Optics 25(16), 2695-2702 (1986).
36. G. Soriano, M. Zerrad, and C. Amra, "Anti-scattering effect analyzed with an exact theory of light scattering from rough multilayers," Opt. Lett. 44(18), 4455-4458 (2019)
37. J. Zhang, S. Fang, I.V. Kozhevnikov, X. Cheng, and Z. Wang, "Interference suppression of light backscattering through oblique deposition of high-reflectivity multilayers: a theoretical analysis," Opt. Express 28(21), 30626-30643 (2020)
38. S. Schroder, T. Herffurth, A. Duparre, and J. E. Harvey, "Impact of surface roughness on scatter losses and the scattering distribution of surfaces and thin film coatings," in Optical Fabrication, Testing, and Metrology Iv, A. Duparre and R. Geyl, eds. (2011), Vol. 8169.
39. M. Zerrad, S. Liukaityte, M. Lequime, and C. Amra, "Light scattered by optical coatings: numerical predictions and comparison to experiment for a global analysis," Appl. Opt. 55(34), 9680 (2016).
40. C. Amra, M. Lequime and M. Zerrad, S. Liukaityte, and M. Lequime, "Instantaneous one-angle white-light scatterometer," Optics Express 26(1), 204-219 (2018).
41. R. A. Probst, T. Steinmetz, T. Wilken, G. K. L. Wong, H. Hundertmark, S. P. Stark, P. S. J. Russell, T. W. Hänsch, R. Holzwarth, and T. Udem, "Spectral flattening of supercontinua with a spatial light modulator," Proc. SPIE 8864, 88641Z (2013).